RSC Advances

PAPER

View Article Online
View Journal | View Issue

Cite this: *RSC Adv.*, 2019, **9**, 15370

The dependence of oxygen sensitivity on the molecular structures of Ir(III) complexes and their application for photostable and reversible luminescent oxygen sensing†

Yang Xing,[a] Chengfang Qiao,[b] Xinmin Li,[c] Chun Li,[a] Honghao Wang,[a] Fayun Li,[a] Ling Di*[ad] and Zhanxu Yang*[a]

Three Ir(III) complexes **IrC1**, **IrC2**, and **IrC3** substituted with 4-(diphenylamino)phenyl (TPA), 4-(9*H*-carbazol-9-yl)phenyl (Cz1), and 9-phenyl-9*H*-carbazol-3-yl (Cz2) moieties were prepared and fully characterized as phosphorescent emitters. In comparison with $Ir(ppy)_3$, introduction of TPA, Cz1, and Cz2 moieties strongly improved the oxygen sensitivities of **IrC1–IrC3**. Short-decayed **IrC1** with I_0/I_{100} of 168.6 and K_{SV}^{app} of 202.2 bar^{-1} in THF exhibited the highest sensitivity for oxygen. TPA and Cz moieties caused remarkable collision radius variations of the Ir(III) complexes with 2.13 ± 0.08 for $\sigma_{IrC1}/\sigma_{Ir(ppy)_3}$, 1.24 ± 0.06 for $\sigma_{IrC2}/\sigma_{Ir(ppy)_3}$, and 1.54 ± 0.08 for $\sigma_{IrC3}/\sigma_{Ir(ppy)_3}$. For demonstrating the dependence of oxygen sensitivity on the molecular structure of the oxygen-sensitive probes (OSPs), the delocalization of spin populations (DSPs) has been applied for the first time to confirm the collision radius variations of Ir(III) complexes. Remarkable DSPs were found on the TPA, Cz1, and Cz2 moieties with the spin population (percentage of the spin population) of 0.23210 (11.61%), 0.08862 (4.43%), and 0.13201 (6.60%), respectively. And strong linear correlations (R^2 = 0.997) between the collision radius variations and spin population on TPA and Cz moieties were apparent. The DSPs could be used to describe the dependence of oxygen sensitivity on the molecular structure of the OSPs. For achieving real-time oxygen sensing, the photostability, oxygen sensing performance, and operational stability of **IrC1–IrC3** and $Ir(ppy)_3$ immobilized in ethyl cellulose (EC) were investigated. The **IrC1**-EC film demonstrated outstanding photostability after 60 min of irradiation and excellent operational stability for continuous oxygen monitoring with no attenuation of the original emission intensity in 4000 s. This study quantified and analyzed the dependence of oxygen sensitivity on the molecular structure of Ir(III) complexes for the first time and illustrated a feasible approach to achieve high-efficiency sensors for real-time monitoring of oxygen.

Received 25th March 2019
Accepted 12th May 2019

DOI: 10.1039/c9ra02277e

rsc.li/rsc-advances

1. Introduction

Oxygen plays an essential role in evolution and reproduction, and is indispensable for all forms of living organisms.[1] The determination of oxygen has attracted special attention in biomedicine and environmental monitoring.[2,3] When compared with traditional methods of oxygen determination (Winkler titration[4] and electroanalytical[5]), luminescent sensing has become extremely significant in the last two decades due to the overwhelming advantages of its nondestructive characteristics, sensitive luminescence response, excellent reversibility, and versatility of formats (film, fiber, nanoparticle, *etc.*).[6] Such type of flexible approach depends on the dynamic (diffusion-controlled) luminescence (phosphorescence or fluorescence) quenching of oxygen-sensitive probes (OSPs).[7,8] The transition metal complexes are OSPs of choice, including Ir(III),[9–12] Pt(II),[13,14] Ru(II)[15,16] complexes, and Pd(II) porphyrins.[17,18]

In general, the oxygen sensitivities of luminescence sensors are roughly proportional to luminescent decay times (τ) of OSPs.[19,20] And state of the art luminescent sensors consisted of OSPs possessing luminescent decay times in a wide range of milliseconds to microseconds.[21] Efforts have been made to design OSPs with long decay times.[8,22,23]

[a]College of Chemistry, Chemical Engineering, and Environmental Engineering, Liaoning Shihua University, Fushun 113001, China. E-mail: diling@lnpu.edu.cn; zxyanglnpu@163.com

[b]College of Chemical Engineering and Modern Materials, Shangluo University, Shangluo 726000, China

[c]School of Pharmacy, Zunyi Medical University, Zunyi, 563000, China

[d]State Key Laboratory of Fine Chemicals, Dalian University of Technology, Linggong Road 2, Dalian 116024, China

† Electronic supplementary information (ESI) available: Phosphorescent emission decay curves and cyclic voltammogram. See DOI: 10.1039/c9ra02277e

Matrices have been widely used to provide microenvironment for OSPs as encapsulation and regulate the determination range of oxygen.[24,25] High oxygen permeability of matrices commonly provided high sensitivity and low limit of detection (LOD).[21,26–28] Luminescent decay times and oxygen sensitivities of OSPs are sometimes not in direct proportion (short-decayed OSPs with high oxygen sensitivities or *vice versa*) in the same matrix with the same approach of preparation. Astoundingly, the abnormal phenomena occurred frequently in the related researches.[9,10,29–31] For instance, Ir(III) complexes Ir(III)-a and Ir(III)-b were immobilized in a nano aluminum based matrix (Scheme 1A). In comparison to short-decayed Ir(III)-a, lower oxygen sensitivity of Ir(III)-b with long decay time was showed.[9] A *t*-butyl substituted Ir(III) complex Ir(III)-d was prepared based on Ir(III)-c (Scheme 1B). The oxygen sensitivity of short-decayed Ir(III)-c was 6-fold higher than that of long-decayed Ir(III)-d.[10] Zhao *et al.* conducted a research on the two Pt(II) complexes Pt(II)-a and Pt(II)-b with phenylthiazo and thiazo-coumarin ligands, respectively (Scheme 1C). And there was a similar phenomenon that short-decayed Pt(II)-a showed considerably high oxygen sensitivity than that of Pt(II)-b.[29] Coincidentally, parallel results were obtained in our previous reports.[32,33] Therefore, the molecular structure of OSPs has potential influence which should not be ignored on the oxygen sensitivity.

Carbazole and triphenylamine moieties have drawn a wide range of attention in organic light-emitting diodes (OLEDs)[34–38] and dye-sensitized solar cells (DSSCs) due to intriguing properties of high light-to-electrical energy conversion efficiencies, strong electron-donating nature and good hole-transporting abilities.[39–41] Herein, we report a systematic quantification and analysis of the dependence of oxygen sensitivity on the molecular structure of OSPs by the modification of traditional Ir(III) complex $Ir(ppy)_3$ with 4-(diphenylamino)phenyl (TPA), 4-(9*H*-carbazol-9-yl)phenyl (Cz1), and 9-phenyl-9*H*-carbazol-3-yl (Cz2) moieties. Molecular structures and synthetic routes of **IrC1**, **IrC2**, **IrC3** and $Ir(ppy)_3$ were illustrated in Scheme 2.

2. Experimental

2.1. Materials and methods

The corresponding boronic acids, $Pd(OAc)_2$, $Pd(PPh_3)_4$, and $IrCl_3 \cdot 3H_2O$ were purchased from Alfa Aesar. Other purified reagents were purchased from Greagent. ^1H NMR and ^{13}C NMR spectra were measured on a BRUKER AVANCE III HD spectrometer (400 MHz). High-resolution MS were measured with a 1290/6224 HPLC/MS spectrometer.[20] The UV/Vis spectrometer (cary 5000) and fluorescence spectrophotometer (cary eclipse G9800A) of Agilent Technology were used to record absorption spectra and emission spectra. The excited-state lifetime curves were recorded on LP920 Laser Flash photolysis apparatus of Edinburgh Instruments Ltd (excitation wavelength: 355 nm, pulse width: 6.4 ns, frequency: 3 Hz, single pulse energy: 1 mJ). The 2273 electrochemical workstation of Princeton Applied Research was used for the cyclic voltammetry tests.

2.2. Synthesis section

Synthetic procedure of ligand L1, L2, and L3. 0.5 mmol of 2-(3-bromophenyl)pyridine (116.5 mg), 0.75 mmol of corresponding boronic acid, 2.0 equiv. of K_2CO_3 (138.0 mg), $Pd(PPh_3)_4$ (5.0 mol%, 0.025 mmol, 28.9 mg), and THF/H_2O (10 mL/6 mL) were mixed and stirred at 85 °C in N_2 for 6 hours. Then 15 mL brine was added into the mixture. Then the mixture was extracted with ethyl acetate (EA, 4 × 10 mL). The organic phase was condensed and the corresponding product was isolated by column chromatography using petroleum ether/EA (50 : 1 for **L1**, 20 : 1 for **L2**, and **L3**, v : v).

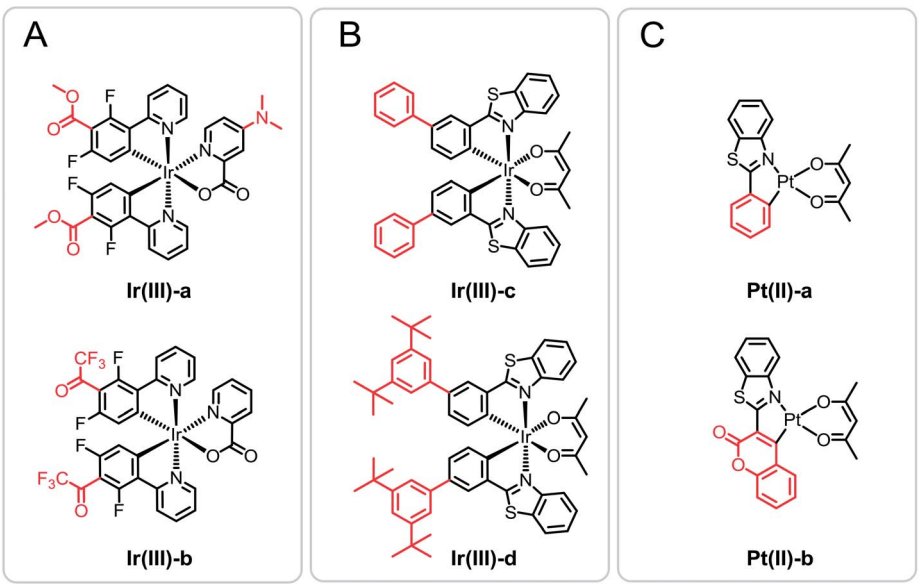

Scheme 1 Chemical structures of referenced Ir(III) and Pt(II) OSPs. Structure variations is shown with red.

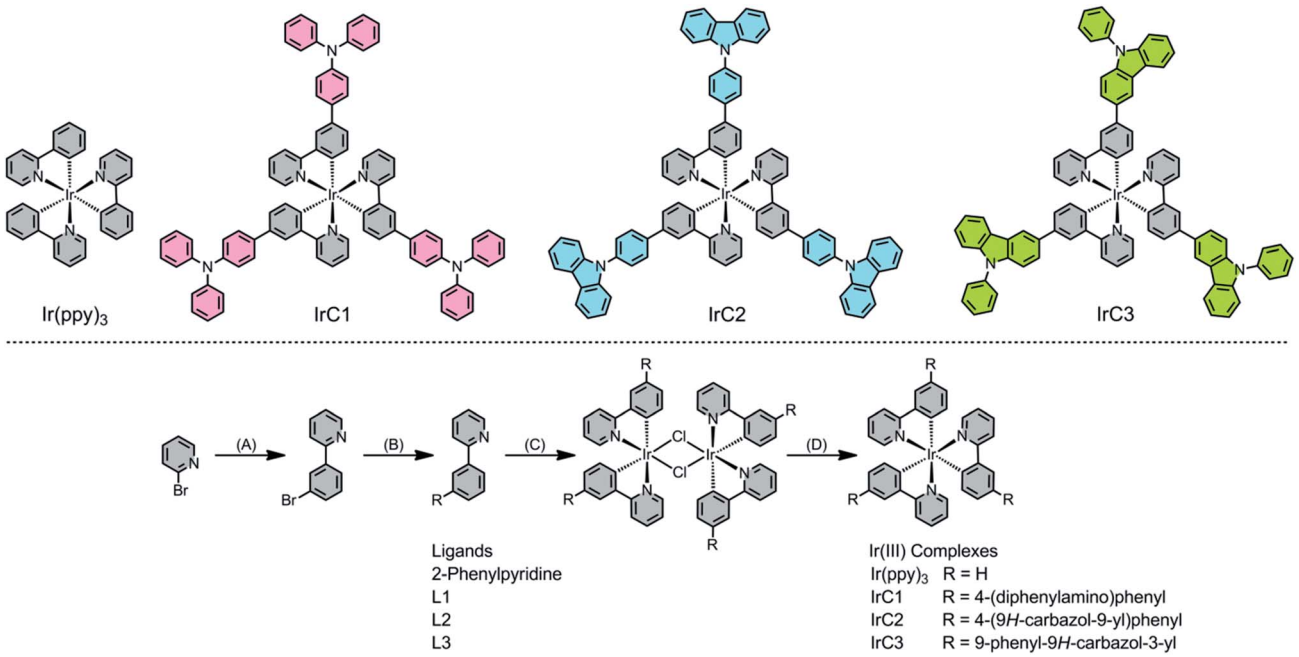

Scheme 2 Molecular structures and synthetic routes of ligands and Ir(III) complexes. (A) (3-Bromophenyl)boronic acid, $Pd(OAc)_2$, K_2CO_3, C_2H_5OH/H_2O (3 : 1, v : v), 85 °C, 3 hours. (B) $RB(OH)_2$, $Pd(PPh_3)_4$, K_2CO_3, THF : H_2O 5 : 3 (v : v), 80 °C in N_2, 6 hours. (C) $IrCl_3 \cdot 3H_2O$, $C_2H_5OCH_2CH_2OH/H_2O$ (3 : 1, v : v), 110 °C in N_2, 36 hours. (D) The corresponding ligands, Na_2CO_3, glycerol, 200 °C in N_2, 48 hours.

L1, *N*,*N*-Diphenyl-3′-(pyridin-2-yl)-[1,1′-biphenyl]-4-amine. Yield: 82.2%; white solid. ^{1}H NMR (400 MHz, $CDCl_3$) δ 8.72 (d, 1H), 8.22 (d, 1H), 7.93 (s, 1H), 7.79 (d, 2H), 7.63 (s, 1H), 7.60–7.50 (m, 3H), 7.27 (s, 5H), 7.17 (s, 3H), 7.15 (s, 3H), 7.05 (d, 2H).[42]

L2, 9-(3′-(Pyridin-2-yl)-[1,1′-biphenyl]-4-yl)-9*H*-carbazole. Yield: 79.1%; white solid. ^{1}H NMR (400 MHz, $CDCl_3$) δ 8.78 (d, 1H), 8.38 (s, 1H), 8.16 (d, 2H), 8.03 (d, 1H), 7.93 (d, 2H), 7.88 (s, 2H), 7.78 (d, 1H), 7.70–7.60 (m, 3H), 7.52–7.40 (m, 4H), 7.31 (t, 3H). ^{13}C NMR (101 MHz, $CDCl_3$) δ 157.1, 149.6, 140.9, 140.8, 140.1, 139.8, 137.1, 137.0, 129.4, 128.7, 127.8, 127.3, 126.2, 125.9, 123.4, 122.4, 120.8, 120.3, 119.9, 109.8. HRMS (ESI): calc. for $C_{29}H_{21}N_2$: 397.1705 $[M + H]^+$. Found: 397.1702 $[M + H]^+$.

L3, 9-Phenyl-3-(3-(pyridin-2-yl)phenyl)-9*H*-carbazole. Yield: 77.2%; white solid. ^{1}H NMR (400 MHz, $CDCl_3$) δ 8.77 (d, 1H), 8.46 (s, 1H), 8.37 (s, 1H), 8.22 (d, 1H), 7.96 (d, 1H), 7.85 (t, 2H), 7.81–7.72 (m, 2H), 7.66–7.56 (m, 5H), 7.52–7.46 (m, 2H), 7.43 (d, 2H), 7.31 (dt, 2H). ^{13}C NMR (101 MHz, $CDCl_3$) δ 157.6, 149.6, 142.6, 141.3, 140.5, 139.8, 137.6, 136.9, 133.2, 129.9, 129.2, 128.0, 127.5, 127.1, 126.1, 126.0, 125.6, 125.2, 123.9, 123.5, 122.2, 120.9, 120.5, 120.1, 119.0, 110.0, 109.9. HRMS (ESI): calc. for $C_{29}H_{21}N_2$: 397.1705 $[M + H]^+$. Found: 397.1703 $[M + H]^+$.

Synthetic procedure of Ir(III) complexes IrC1, IrC2, and IrC3. The corresponding ligand 0.8 mmol (**L1** 318.4 mg, **L2** 316.8 mg, **L3** 316.8 mg, respectively) was reacted with 0.6 equiv. of $IrCl_3 \cdot 3H_2O$ (0.48 mmol, 169 mg) in $C_2H_5OCH_2CH_2OH/H_2O$ (12 mL/4 mL) at 110 °C for 36 h under N_2. The solution was condensed to afford a powder of iridium chloride-bridged dimer. Without purification, the dimer was reacted with 1.2 equiv. (0.48 mmol) corresponding ligand (**L1** 191 mg, **L2** 190 mg, **L3** 190 mg, respectively) and 5 equiv. of Na_2CO_3 (4 mmol, 424 mg) in 25 mL glycerol at 200 °C for 2 days under N_2. Upon cooling to room temperature, the mixture was poured into water and extracted with CH_2Cl_2 (3 × 25 mL). The organic phase was condensed and the corresponding product was isolated by column chromatography using dichloromethane.[33]

IrC1: yield: 77.4%; yellow powder. ^{1}H NMR (400 MHz, $CDCl_3$) δ 7.96 (s, 3H), 7.86 (s, 3H), 7.64–7.57 (m, 6H), 7.50 (s, 3H), 7.48 (d, 3H), 7.23 (s, 6H), 7.20 (s, 3H), 7.12 (s, 12H), 7.10–7.02 (m, 12H), 7.00 (s, 3H), 6.99–6.94 (m, 6H), 6.91–6.86 (m, 3H). ^{13}C NMR (101 MHz, $CDCl_3$) δ 169.7, 167.6, 146.9, 143.2, 142.9, 139.3, 136.8, 136.4, 136.1, 131.2, 130.1, 129.1, 128.4, 125.3, 123.9, 123.1, 121.2, 121.0, 118.5. HRMS (ESI) for $C_{87}H_{64}IrN_6$, calc.: 1385.4822 $[M + H]^+$. Found: 1385.4820 $[M + H]^+$.[42]

IrC2: yield: 70.4%; yellow powder. ^{1}H NMR (400 MHz, $CDCl_3$) δ 8.14 (t, 9H), 8.05 (t, 6H), 7.88 (d, 6H), 7.68 (d, 6H), 7.63–7.57 (m, 6H), 7.49–7.39 (t, 18H), 7.30 (d, 6H). ^{13}C NMR (101 MHz, $CDCl_3$) δ 166.2, 150.2, 141.3, 141.1, 138.6, 137.8, 135.4, 135.0, 129.7, 129.2, 128.4, 127.9, 127.0, 125.3, 122.4, 121.3, 120.2, 119.6, 119.1, 108.4. HRMS (ESI) for $C_{87}H_{58}IrN_6$, calc.: 1379.4352 $[M + H]^+$. Found: 1379.4347 $[M + H]^+$.

IrC3: yield: 75.2%; yellow powder. ^{1}H NMR (400 MHz, $CDCl_3$) δ 8.39 (s, 3H), 8.17 (d, 6H), 8.10 (d, 6H), 8.05 (s, 6H), 7.68 (d, 6H), 7.60 (d, 12H), 7.47–7.39 (m, 12H), 7.30 (d, 6H). ^{13}C NMR (101 MHz, $CDCl_3$) δ 167.5, 150.8, 143.3, 142.9, 140.1, 138.8, 136.7, 135.4, 134.4, 133.3, 130.0, 128.8, 127.7, 126.3, 125.9, 124.8, 124.2, 122.7, 122.5, 121.8, 121.3, 119.3, 118.8,

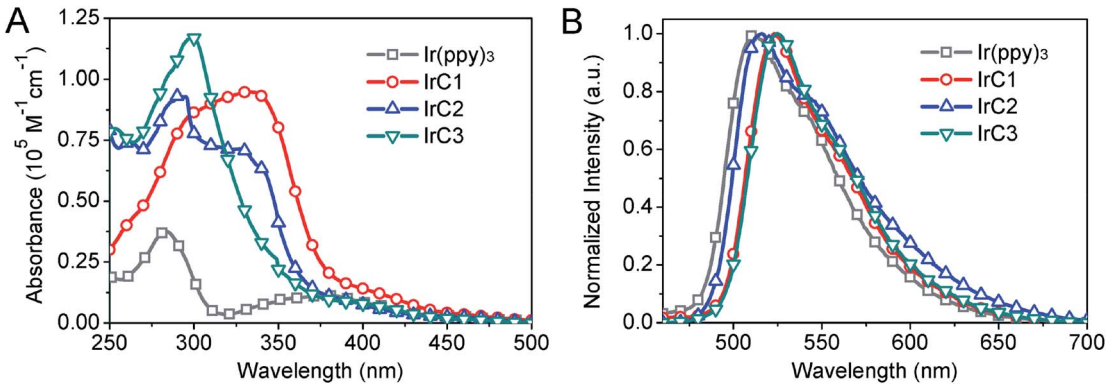

Fig. 1 (A) UV-vis spectra and (B) luminescent spectra of **IrC1–IrC3** and $Ir(ppy)_3$.

Table 1 Photophysical parameter of **IrC1–IrC3** and $Ir(ppy)_3$

	Absorption [a]	Emission [b]				
Complexes	λ_{abs} (nm) (ε, 10^4 mol L^{-1} cm^{-1})	λ_{em} (nm)	τ (μs) [c]	Φ_p [d]	k_r (10^5 s^{-1}) [e]	k_{nr} (10^5 s^{-1}) [f]
$Ir(ppy)_3$	284 (3.75), 379 (1.12), 411 (0.71), 456 (0.27), 490 (0.12)	511	2.38	0.40	1.68	2.52
IrC1	332 (9.48), 404 (1.32), 472 (0.27)	522	2.42	0.53	2.19	1.94
IrC2	290 (9.31), 327 (7.15), 340 (6.34), 389 (0.95), 447 (0.25)	516	2.76	0.50	1.81	1.81
IrC3	299 (11.69), 349 (2.62), 397 (0.82), 421 (0.51)	525	3.19	0.50	1.57	1.56

[a] In THF at a concentration of 10^{-5} mol L^{-1}. [b] In degassed THF. [c] $\lambda_{ex} = 355$ nm. [d] Relative to $Ir(ppy)_2(acac)$ ($\Phi_p = 0.34$). [e] $k_r = \Phi_p/\tau$. [f] $k_{nr} = (1/\tau) - k_r$.

117.7, 117.1, 108.8, 108.7. HRMS (ESI) for $C_{87}H_{58}IrN_6$, calc.: 1379.4352 $[M + H]^+$. Found: 1379.4342 $[M + H]^+$.

3. Result and discussion

3.1. Photophysical properties

UV-visible absorption of **IrC1–IrC3** and $Ir(ppy)_3$ have been measured in THF at room temperature (Fig. 1A and Table 1). Strong bands up to 310 nm attributed to π–π* transitions of intraligands. Bands of lower-energy absorption at 350 nm were assigned to metal-to-ligand charge transfer transitions (MLCT). The spin-forbidden transitions of triplet states ascribed to weak bands at 400 nm with absorption coefficients of 2000 M^{-1} cm^{-1}. The similar band positions and significant differences of absorption coefficients of **IrC1–IrC3** and $Ir(ppy)_3$ were observed. In comparison with $Ir(ppy)_3$, intensity of the first band at 280 nm and the second band at 350 nm of **IrC1–IrC3** were enhanced which was attributed to π–π* transition and MLCT of intraligands. It is probably due to the enhanced delocalization of the excited electron on TPA, Cz1, and Cz2 moieties which was confirmed by theoretical calculations (Fig. 2).[43]

The emission maxima were in region from 511 to 525 nm which was excited in the MLCT bands (Fig. 1B and Table 1). In comparison to $Ir(ppy)_3$ (511 nm), introduction of TPA and Cz moieties showed bathochromic shift of emission maxima of **IrC1** (522 nm), **IrC2** (516 nm), and **IrC3** (525 nm). The emission maxima of **IrC1** was shifted to a longer wavelength by TPA moieties. The phosphorescence quantum yields (Φ_p) of **IrC1** (0.53), **IrC2** (0.50), **IrC3** (0.50) were enhanced compared to $Ir(ppy)_3$ (0.40) (Table 1). The luminescent decay times (τ) were in the sequence of **IrC3** (3.19 ± 0.02 μs) > **IrC2** (2.76 ± 0.01 μs) > **IrC1** (2.42 ± 0.03 μs) > $Ir(ppy)_3$ (2.38 ± 0.02 μs). The τ in microseconds inferred that the emissions were phosphorescent (Table 1 and Fig. S1, see ESI†).[44] Radiative (k_r) and nonradiative (k_{nr}) decay rates were calculated by Φ_p and τ. And the radiative lifetimes $\tau_{rad}(1/k_r)$ for **IrC1–IrC3** and $Ir(ppy)_3$ were 4.57 μs, 5.52 μs, 6.40 μs, and 5.95 μs, respectively (Table 1). Compared to **IrC1**, the extended τ_{rad} of **IrC2** and **IrC3** was possibly attributed to enhanced conjugation effects which was caused by Cz moieties.[45] The changes in emission color were quantified with CIE coordinates of (0.2750, 0.6268) for $Ir(ppy)_3$, (0.3164, 0.6341) for **IrC1**, (0.3286, 0.6090) for **IrC2**, and (0.3242, 0.6332) for **IrC3** (Fig. S2, see ESI†).

3.2. Electrochemical properties

The electrochemical behaviors of **IrC1–IrC3** and $Ir(ppy)_3$ were studied by cyclic voltammetry (Table 2). The introduction of TPA moieties leaded to more negative oxidation potential (0.78 V) and higher HOMO energy level (−5.18 eV) of **IrC1**. And the introduction of Cz moieties showed more obvious cathodic shifts of oxidation potentials of **IrC2** (0.72 V) and **IrC3** (0.67 V) in comparison with $Ir(ppy)_3$ (0.84 V). $Ir(ppy)_3$

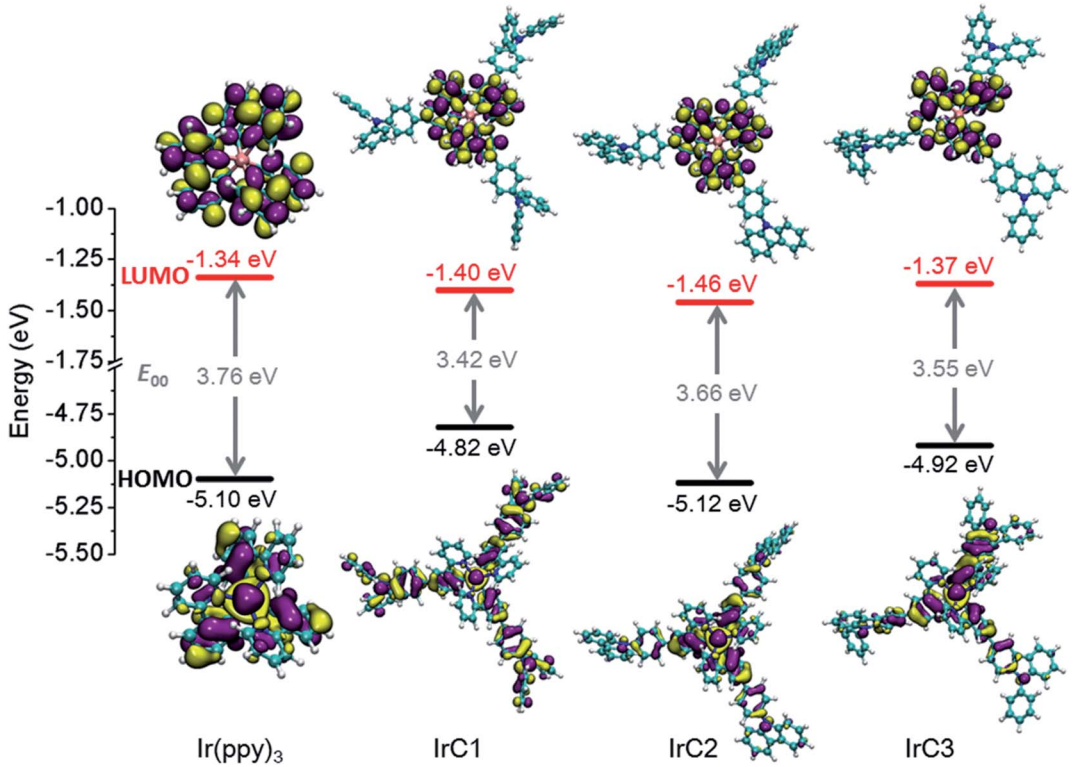

Fig. 2 Electron density isosurfaces (0.02 a.u.) of frontier molecular orbitals of Ir(III) complexes.

Table 2 Electrochemical data and frontier orbital energy levels of **IrC1–IrC3** and $Ir(ppy)_3$

Ir(III) complexes	$E_{ox}^{on\ set}$ [a] (V)	E_{HOMO} [b] (eV)	E_{LUMO} [c] (eV)	λ_{edge} [d] (nm)	E_{00} [e] (eV)	E_{ox}^{*} (V) [f]
$Ir(ppy)_3$	0.84	−5.24	−2.96	544	2.28	−1.44
IrC1	0.78	−5.18	−3.02	574	2.16	−1.38
IrC2	0.72	−5.12	−2.89	556	2.23	−1.51
IrC3	0.67	−5.07	−2.96	587	2.11	−1.44

[a] Onset oxidation potential. 0.1 mol L^{-1} $[Bu_4N]PF_6$ was dissolved in degassed THF. The standard electrode was SCE. [b] HOMO energy level, E_{HOMO} (eV) $= -e(4.4 + E_{ox}^{on\ set})$. [c] LUMO energy level, $E_{LUMO} = E_{HOMO} + E_{00}$. [d] Absorption edge data, which were measured from solid UV-vis spectra. [e] Zero–zero emission energy level. $E_{00} = 1240/\lambda_{edge}$. [f] Oxidation potential of excited state: $E_{ox}^{*} = E_{ox}^{on\ set} - E_{00}$.[46]

and **IrC1** demonstrated quasi-reversible reduction waves, which exhibited electrochemical stability and relative difficulty of oxidation. While **IrC2** and **IrC3** showed irreversible reduction waves (Fig. S3, see ESI†). Therefore all the HOMO energy levels were calculated by the onset oxidation potentials ($E_{ox}^{on\ set}$) (Table 2). The data of zero–zero emission energy levels (E_{00}) were calculated by the absorption edge data (λ_{edge}) of solid UV-vis spectra (Fig. S4, see ESI†). The data of E_{00} with order of $Ir(ppy)_3$ (2.28 eV) > **IrC2** (2.23 eV) > **IrC1** (2.16 eV) > **IrC3** (2.11 eV) were in accordance with the order of emission maxima in Fig. 1B.

3.3. Theoretical calculations

Density functional theory (DFT) calculations (B3LYP level, mixed basis sets of 6-31G* and LanL2DZ) based on the polarizable continuum model (PCM = THF) were applied to optimize the ground-state geometries of Ir(III) complexes[20] (Fig. 2). TPA moieties of **IrC1** take no-co-planar geometry. Contrastively, large π-conjugation were presented on Cz1 and Cz2 moieties of **IrC2** and **IrC3** just as expected. It was clear that 2-phenylpyridine moieties significantly contributed the LUMOs of **IrC1–IrC3** and $Ir(ppy)_3$. And none of electron population on Ir(III) atom, TPA, and Cz moieties of LUMOs. Ir(III) atoms and benzene rings of 2-phenylpyridines mainly contributed the HOMOs, while pyridine rings slightly contributed the HOMOs. The electron delocalization was increased on the propeller structures of **IrC1**. While the π-conjugation reduced the electron delocalization on Cz moieties of HOMOs of **IrC2** and **IrC3**. These frontier molecular orbital energies in Fig. 2 and Table 2 were not over-interpreted

because of acceptable differences between experimental and calculated data.[47]

3.4. Luminescence sensing of molecular oxygen

The Stern–Volmer relationship (eqn (1)) described the diffusion-controlled luminescent quenching process between OSPs and oxygen. I and τ are emission intensities and luminescent decay times of OSPs, respectively. I_0 and τ_0 are corresponding values in the absence of oxygen. k_q means the bimolecular quenching constant and $[O_2]$ expresses the molar concentration of molecular oxygen. The Stern–Volmer plots (SVPs) are gotten with slopes of $k_q\tau_0$ by linear fitting.

$$\frac{I_0}{I} = \frac{\tau_0}{\tau} = 1 + k_q\tau_0[O_2] \quad (1)$$

In order to drastically eliminate the influence of heterogeneity and accurately characterize original oxygen sensitivities, purified THF was used to disperse Ir(III) complexes. The emission intensities of **IrC1–IrC3** and $Ir(ppy)_3$ were obviously weaken with incremental concentration of O_2 in the air volume of 0–100%. 6.8% of oxygen concentration could quench over 81% of original emission intensities. Noteworthily, above 90% of original emission intensity of **IrC1** was quenched with 6.8% of oxygen which demonstrated high oxygen sensitivity (Fig. 3).

The two-site model[48] was applied to fit the SVPs (eqn (2)). Where f_1 and f_2 are the quenchable and unquenchable fractions, respectively. And K_{SV1} and K_{SV2} are quenching rate constants for corresponding fractions. $f_1 + f_2 = 1$. p_{O_2} means oxygen partial pressure. Oxygen sensitivities of OSPs are illustrated by the weighted constant K_{SV}^{app} ($K_{SV}^{app} = f_1K_{SV1} + f_2K_{SV2}$).

$$\frac{I}{I_0} = \frac{\tau}{\tau_0} = \frac{f_1}{1 + K_{SV1}p_{O_2}} + \frac{f_2}{1 + K_{SV2}p_{O_2}} \quad (2)$$

Decline ratios of emission intensity of **IrC1–IrC3** and $Ir(ppy)_3$ were fitted by the two-site model in Fig. 4 and Table S1 (see ESI†). The I_0/I_{100} of **IrC1–IrC3** and $Ir(ppy)_3$ were 168.6, 115.1, 158.1, and 79.4, respectively. And K_{SV}^{app} of **IrC1–IrC3** and $Ir(ppy)_3$ were 202.2 bar^{-1}, 144.1 bar^{-1}, 181.1 bar^{-1}, and 119.6 bar^{-1}. **IrC1** demonstrated the highest oxygen sensitivity than others. The oxygen sensitivities were in the order of **IrC1** > **IrC3** > **IrC2** > $Ir(ppy)_3$. Hence, introducing TPA and Cz moieties distinctly made Ir(III) complexes more sensitive to oxygen. Noticeably, large quenchable portions (f_1) of **IrC1** (0.998), **IrC2** (0.999), and **IrC3** (0.999) were improved compared with that of $Ir(ppy)_3$ (0.985), which demonstrated considerable linearity of SVPs and more homogeneous

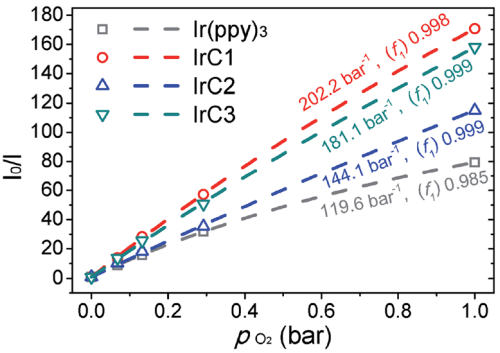

Fig. 4 SVPs for **IrC1–IrC3** and $Ir(ppy)_3$ in THF (fitted by two-site model).

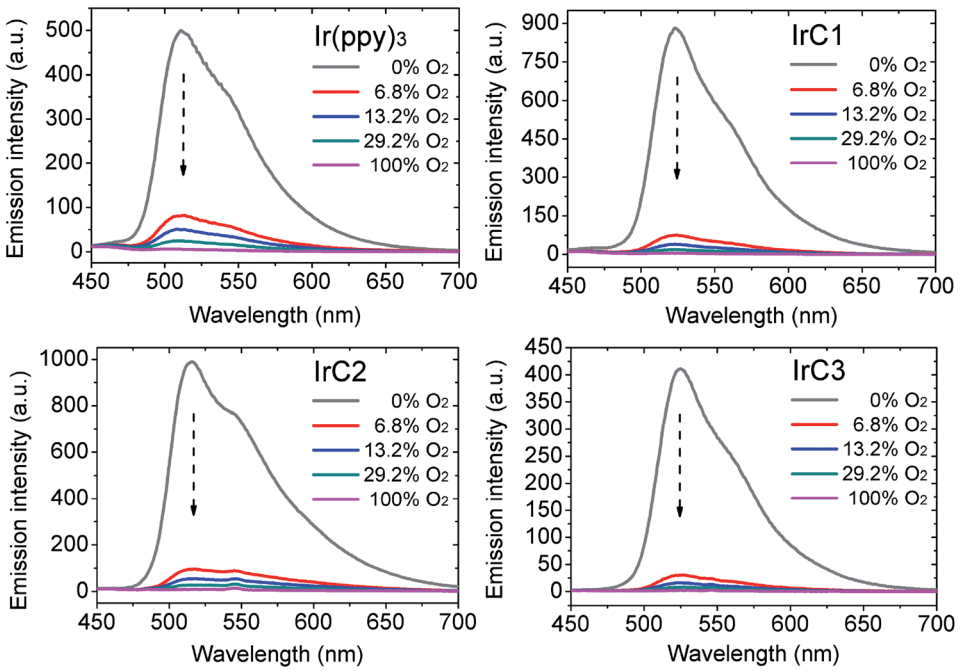

Fig. 3 Dependence of luminescent spectra of Ir(III) complexes in THF (10^{-5} mol L^{-1}) of 0–100% O_2.

microenvironment. The limit of detections (LODs) of **IrC1–IrC3** and $Ir(ppy)_3$ in THF were 0.27 mbar, 0.40 mbar, 0.28 mbar, and 0.43 mbar, respectively (see ESI†).

3.5. Variations of the collision radius

Winnik *et al.* reported the fundamental expression of luminescent oxygen sensing (eqn (3)).[7] In eqn (3), P_{O_2} means oxygen permeability of solvents or matrices. N_A means the constant of Avogadro. α expresses the constant of luminescent quenching probability. σ represents the collision radii of OSPs to molecular oxygen. In eqn (3), P_{O_2} describes the dependence of oxygen sensitivity on matrices. And high values of P_{O_2} caused high oxygen sensitivities of OSPs.[26] τ_0 illustrates the dependence of oxygen sensitivity on the photophysical properties of OSPs. Long-lived τ_0 leaded to high oxygen sensitivities of OSPs.[19,21] The variations of collision radii (σ) describe the dependence of oxygen sensitivity on molecular structures of OSPs. OSPs with high values of σ should be more sensitive to oxygen.

$$\frac{I_0}{I} = \frac{\tau_0}{\tau} = 1 + \frac{4\pi\alpha N_A}{1000}(P_{O_2})(\sigma\tau_0)p_{O_2} \quad (3)$$

According to eqn (3), the ratio of collision radii (σ_1/σ_2) between two OSPs was obtained by the expression (eqn (4)), reads as

$$\frac{\sigma_1}{\sigma_2} = \frac{\left[\left(\frac{I_0}{I}\right)_1 - 1\right]\tau_2}{\left[\left(\frac{I_0}{I}\right)_2 - 1\right]\tau_1} \quad (4)$$

The ratios of collision radii between **IrC1–IrC3** and $Ir(ppy)_3$ ($\sigma_{Ir(III)}/\sigma_{Ir(ppy)_3}$) represented the collision radius variations of OSPs. With luminescent decay times, the $\sigma_{Ir(III)}/\sigma_{Ir(ppy)_3}$ have been calculated by measuring data of I_0 and I_{100} five times in parallel (Table S2, see ESI†). The ratios of collision radii were 2.13 ± 0.08 for $\sigma_{IrC1}/\sigma_{Ir(ppy)_3}$, 1.24 ± 0.06 for $\sigma_{IrC2}/\sigma_{Ir(ppy)_3}$, and 1.54 ± 0.08 for $\sigma_{IrC3}/\sigma_{Ir(ppy)_3}$, respectively, with the sequence of **IrC1** > **IrC3** > **IrC2** > $Ir(ppy)_3$ (Fig. 5). In contrast to $Ir(ppy)_3$, σ of **IrC1** was obviously increased by TPA moieties. And in comparison with **IrC1**, the introduction of Cz1 and Cz2 moieties markedly decreased the collision radii of **IrC2** and **IrC3**, respectively.

In this research, the delocalization of spin populations (DSPs) was for the first time applied to confirm the collision radius variations of Ir(III) complexes. The spin densities of T_1-state **IrC1–IrC3** and $Ir(ppy)_3$ were calculated using unrestricted DFT calculations (B3LYP level, mixed basis sets of 6-31G* and LanL2DZ) (Fig. 6 and Table S3, see ESI†).[49,50] The spin-density contours of **IrC1–IrC3** and $Ir(ppy)_3$ were dominated by p orbitals with spin population P_{spin} (percentages of

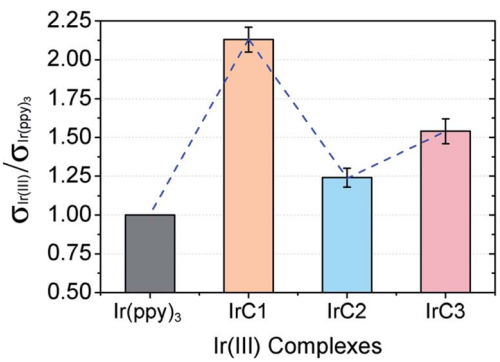

Fig. 5 The ratios of collision radii for **IrC1–IrC3** *versus* $Ir(ppy)_3$.

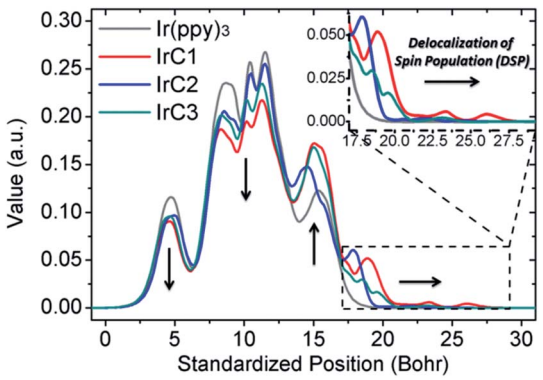

Fig. 7 Spin-density integral curves of the optimized T_1-state geometry of **IrC1–IrC3** and $Ir(ppy)_3$ along the *Z* axis.

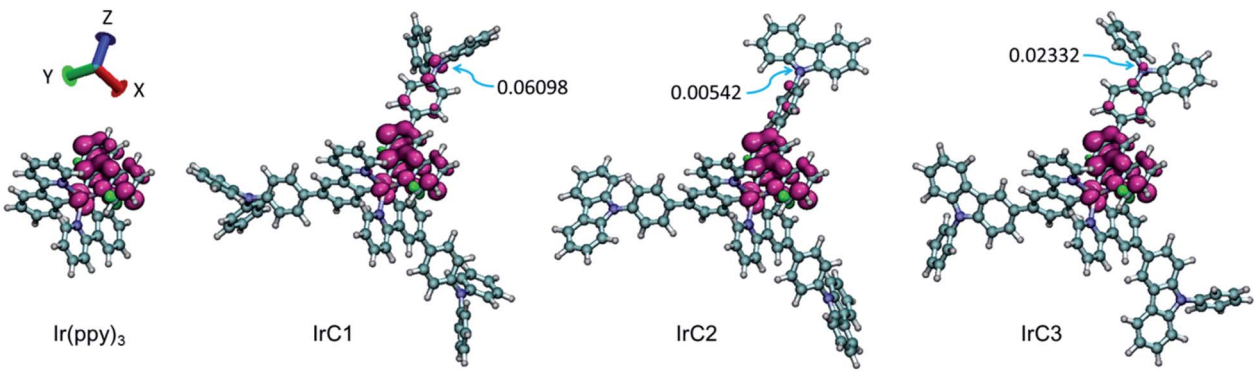

Fig. 6 Spin-density contours (0.003 a.u.) of **IrC1–IrC3** and $Ir(ppy)_3$. Magenta and green contours mean positive and negative phase. Arrows exhibited the spin population variations of on N atoms.

spin population, $P_{spin\%}$) of 1.66310 (83.15%), 1.59881 (79.94%), 1.62016 (81.00%) and 1.55760 (77.88%), respectively. One of intraligands of Ir(III) complexes significantly contributed the spin-orbital contours. Remarkable DSPs were found on the TPA, Cz1, and Cz2 moieties with P_{spin} ($P_{spin\%}$) of 0.23210 (11.61%), 0.08862 (4.43%), and 0.13201 (6.60%), respectively (Table S3, see ESI†). TPA moieties caused more intense DSPs than Cz moieties. The DSPs could be visually observed on the spin-density contours of N atoms on TPA, Cz1, and Cz2 moieties with P_{spin} of 0.06098, 0.00542, and 0.02332, respectively (Fig. 6). The spin-density integral curves of **IrC1–IrC3** and $Ir(ppy)_3$ were plotted along Z axis (Fig. 7).[49] Compared with $Ir(ppy)_3$, spin population on Ir(III) atoms and 2-phenylpyridine moieties of **IrC1–IrC3** declined in the range of 0 to 13 bohr, and then increased from 13 bohr to 27.5 bohr which exhibited intense DSPs on TPA, Cz1, and Cz2 moieties. Notably, considerable DSPs were demonstrated on TPA moieties than Cz1 and Cz2 moieties in the range of 17.5 to 27.5 bohr (Fig. 7). The integral curves confirmed the collision radius variations of Ir(III) complexes in Fig. 5.

To demonstrate the relationship between the collision radius variations and the DSPs of Ir(III) complexes. The ratios of collision radii ($\sigma_{Ir(III)}/\sigma_{Ir(ppy)_3}$) and the spin population (P_{spin}) on TPA, Cz1, and Cz2 moieties of **IrC1–IrC3** were fitted with linearity (Fig. 8). Strong linear correlations between the ratios of collision radii and P_{spin} were apparent with R^2 of 0.997. Hence, the DSPs could be the descriptor for the dependence of oxygen sensitivity on the molecular structure of Ir(III) complexes. In comparison with $Ir(ppy)_3$, introduction of TPA and Cz moieties effectively improved the DSPs on intraligands resulting in increase of collision radii of Ir(III) complexes. Despite the upward tendency of luminescent

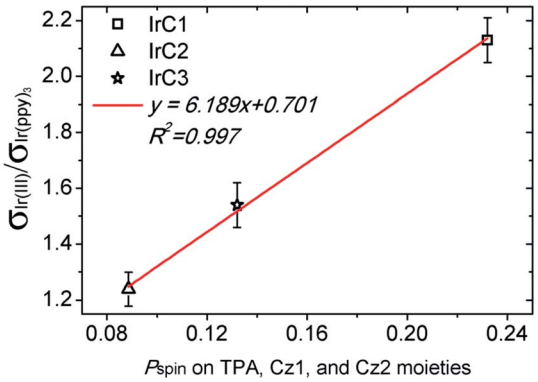

Fig. 8 The linear fitting curve between the ratios of collision radii ($\sigma_{Ir(III)}/\sigma_{Ir(ppy)_3}$) and the spin population (P_{spin}) of **IrC1–IrC3**.

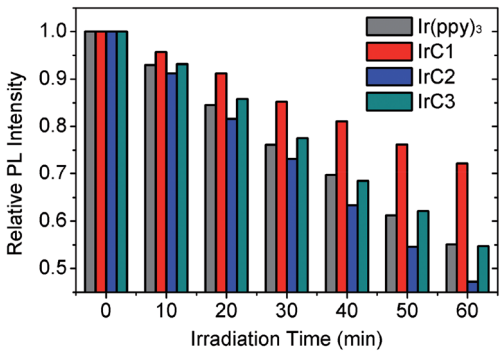

Fig. 10 Luminescent attenuation of Ir(III) films under continuous irradiation.

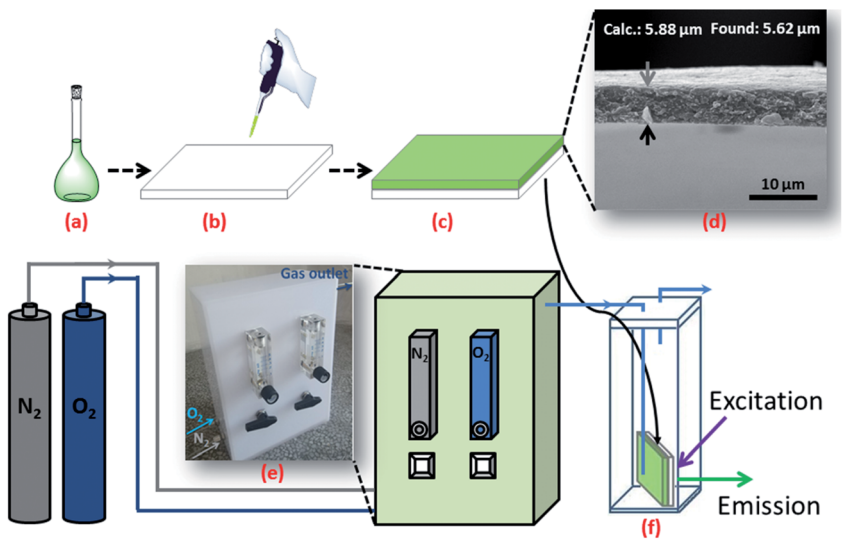

Fig. 9 Schematic illustration for the fabrication of **IrC1**-EC film (0.5 wt%) as sample and oxygen sensing measurements. (a) EC (9.95 mg) and THF (0.90 mL) were mixing with 0.10 mL **IrC1**-THF solution (0.5 mg mL^{-1}). (b) The mixture (0.10 mL) was painted on a vitreous quartz sheet ($S = 1.54$ mm^2). (c) For the formation of the thin film, the solution was volatilized for 1 day at room temperature. (d) The SEM cross profile of **IrC1**-EC film. (e) Two tube flowmeters for the mixture of oxygen and nitrogen. (f) The **IrC1**-EC film on the vitreous quartz sheet was put in a cuvette for oxygen sensing measurements.

decay times from **IrC1** to **IrC3**, the increase of collision radius of **IrC1** resulted in outstanding oxygen sensitivity.

3.6. Photostability measurements

The photostability of OSPs is always of great concern for practical applications such as high-light densities determination or long-time continuous monitoring of oxygen. In this work, easily available supporting matrix ethyl cellulose (EC) was applied to immobilize Ir(III) complexes, respectively (Fig. 9a–c). The thickness of EC films is 5.62 μm (Fig. 9d). Ir(III) films were irradiated with Xe lamp under high power density of 27.3 W m^{-2} in air. And photostabilities of Ir(III) films were measured in N_2 every 10 minutes.[51] The data in Fig. 10 indicated that emission intensities of Ir(III) films were attenuated through continuous irradiation. **IrC1** demonstrated higher photostability than that of $Ir(ppy)_3$, **IrC2** and **IrC3**. About 27.8% of **IrC1**, 52.8% of **IrC2**, 45.3% of **IrC3**, and 44.9% of $Ir(ppy)_3$ were destroyed after 60 min of irradiation. The photostabilities were in the sequence of **IrC1** > $Ir(ppy)_3$ ≈ **IrC3** > **IrC2**. And the sequence was correlated well with the order of excited-state oxidation potentials (E^*_{ox}) in Table 2, which determined the photo-oxidation reactivity of OSPs.[46] Thus, the introduction of TPA moieties raises E^*_{ox} which makes **IrC1** more stable to continuous irradiation.

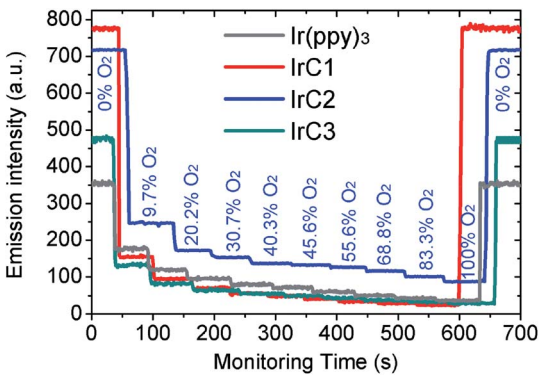

Fig. 11 Time-dependent luminescent responses of Ir(III) films with incremental concentration of oxygen.

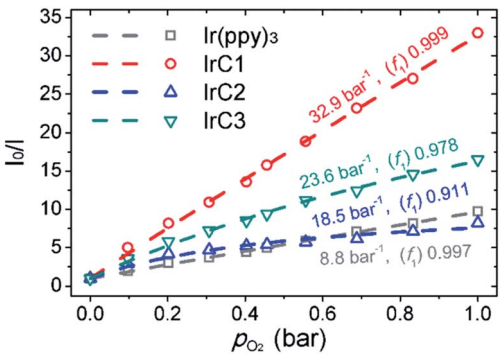

Fig. 12 SVPs for Ir(III) oxygen sensing films (fitted by two-site model).

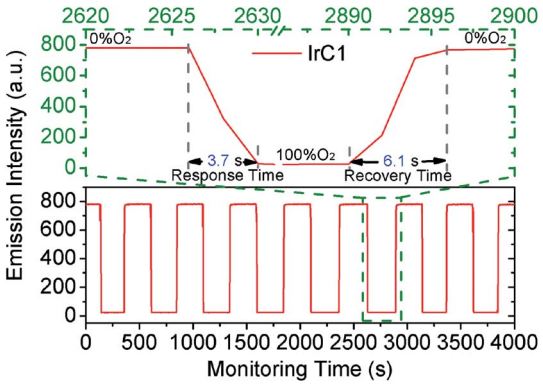

Fig. 13 Reversibility trace curve of **IrC1**-EC film to 0% O_2/100% O_2 saturation cycles in 4000 s.

3.7. Real-time monitoring of oxygen

The luminescent responses of Ir(III) films were studied by gradually increasing concentration of O_2. The Ir(III) films in 0% O_2 (100% N_2) exhibited intense room-temperature phosphorescence. And emission intensities of Ir(III) films were attenuated stepwise with incremental concentration of O_2 (Fig. 11). K^{app}_{SV} and f_1 values were summarized in Fig. 12 and Table S4 (see ESI†) which were fitted by eqn (2). The I_0/I_{100} for Ir(III) films of **IrC1**, **IrC2**, **IrC3**, and $Ir(ppy)_3$ were 33.0, 8.2, 16.5, and 9.7 with K^{app}_{SV} of 32.9 bar^{-1}, 18.5 bar^{-1}, 23.6 bar^{-1} and 8.8 bar^{-1}. The **IrC1**-EC film exhibited outstanding oxygen sensitivity than that of other films. And the sequence of oxygen sensitivities was **IrC1** > **IrC3** > **IrC2** > $Ir(ppy)_3$, which was consistent with the sequence of oxygen sensitivities in THF (Fig. 4). The f_1 values of **IrC1** (0.999), **IrC3** (0.978), and $Ir(ppy)_3$ (0.997) films were higher than that of **IrC2** (0.911) which showed considerable linearity and perfect microhomogeneity and resulted in increased oxygen sensitivities.

3.8. Operational stability of oxygen sensing film

Because of the excellent oxygen sensing performance and high photostability, the operational stability of **IrC1**-EC film was measured by switching O_2 and N_2 atmospheres in 4000 s (Fig. 13). The values of I_0 and I_{100} was constant and the cycles of quenching and recovery were perfectly reversible with no attenuation of original emission intensity which exhibited excellent operational stability. The response time of 3.7 s and recovery time of 6.1 s (96.6% recovery of original intensity) indicated quick responses of **IrC1**-EC film to molecular oxygen. Therefore, **IrC1**-EC film demonstrated outstanding photostability and operational stability which satisfied online continuous monitoring of molecular oxygen.

4. Conclusions

In summary, new TPA and Cz moieties contained Ir(III) complexes **IrC1**, **IrC2**, and **IrC3** were prepared and fully characterized as OSPs for luminescent sensing of oxygen. The ratios of collision radii ($\sigma_{Ir(III)}/\sigma_{Ir(ppy)_3}$) of **IrC1–IrC3** to $Ir(ppy)_3$ were 2.13 ± 0.08, 1.24 ± 0.06, and 1.54 ± 0.08, respectively. Remarkable

DSPs were found on the TPA, Cz1, and Cz2 moieties with the spin population (percentages of spin population) of 0.23210 (11.61%), 0.08862 (4.43%), and 0.13201 (6.60%), respectively. Strong linear correlations between the ratios of collision radii ($\sigma_{Ir(III)}/\sigma_{Ir(ppy)_3}$) and the spin population on TPA and Cz moieties of **IrC1–IrC3** were apparent with R^2 of 0.997. The DSPs could be used to describe the dependence of oxygen sensitivity on the molecular structure of Ir(III) complexes. Introduction of TPA moieties could strongly improve photostability of Ir(III) complexes to reduce photo-oxidation. And fast response and recovery times of **IrC1**-EC film were obtained at 3.7 s and 6.1 s with no attenuation of original emission intensity in 4000 s which exhibited the excellent reversibility and operational stability. The results provide new concepts and technical supports for the design of high-performance luminescent sensors for monitoring of oxygen.

Conflicts of interest

There are no conflicts to declare.

Acknowledgements

The author thank the financial supports of Liaoning Shihua University (2017XJJ-001, 2016XJJ-099), the Education Department of Liaoning Province (L2017LQN007), the National Natural Science Foundation of China (21703135), and the Natural Science Foundation of the Department of Education of Shaanxi Province (17JS034).

Notes and references

1 P. Di Mascio, G. R. Martinez, S. Miyamoto, G. E. Ronsein, M. H. G. Medeiros and J. Cadet, *Chem. Rev.*, 2019, **119**, 2043.
2 M. Quaranta, S. M. Borisov and I. Klimant, *Bioanal. Rev.*, 2012, **4**, 115.
3 D. B. Papkovsky and R. I. Dmitriev, *Chem. Soc. Rev.*, 2013, **42**, 8700.
4 K. Iman and M. Shahid, *New J. Chem.*, 2019, **43**, 1094.
5 X. Zhang, L. Huang, Q. Wang and S. Dong, *J. Mater. Chem. A*, 2017, **5**, 18839.
6 X. D. Wang and O. S. Wolfbeis, *Chem. Soc. Rev.*, 2014, **43**, 3666.
7 X. Lu and M. A. Winnik, *Chem. Mater.*, 2001, **13**, 3449.
8 Y. Amao, *Microchim. Acta*, 2003, **143**, 1.
9 M. Marín-Suárez, B. F. E. Curchod, I. Tavernelli, U. Rothlisberger, R. Scopelliti, I. Jung, D. Di Censo, M. Grätzel, J. F. Fernández-Sánchez, A. Fernández-Gutiérrez, M. K. Nazeeruddin and E. Baranoff, *Chem. Mater.*, 2012, **24**, 2330.
10 M. Li, B. Zheng, D. Luo, H. Sun, N. Wang, Y. Huang, J. Dai, D. Xiao, S.-J. Su and Z. Lu, *Chem. Commun.*, 2015, **51**, 1926.
11 V. Y. Vasilyev, N. B. Morozova, T. V. Basova, I. K. Igumenov and A. Hassan, *RSC Adv.*, 2015, **5**, 32034.
12 P. Majumdar, X. Yuan, S. Li, B. Le Guennic, J. Ma, C. Zhang, D. Jacquemin and J. Zhao, *J. Mater. Chem. B*, 2014, **2**, 2838.
13 L. Liu, D. Huang, S. M. Draper, X. Yi, W. Wu and J. Zhao, *Dalton Trans.*, 2013, **42**, 10694.
14 C. Arunkumar, F. R. Kooriyaden, X. Zhang, S. Sujatha and J. Zhao, *New J. Chem.*, 2017, **41**, 4908.
15 H. Guo, L. Zhu, C. Dang, J. Zhao and B. Dick, *Phys. Chem. Chem. Phys.*, 2018, **20**, 17504.
16 K. Xu, J. Zhao and E. G. Moore, *Photochem. Photobiol. Sci.*, 2016, **15**, 995.
17 Y. Che, W. Yang, G. Tang, F. Dumoulin, J. Zhao, L. Liu and Ü. İşci, *J. Mater. Chem. C*, 2018, **6**, 5785.
18 S. M. Borisov, G. Nuss, W. Haas, R. Saf, M. Schmuck and I. Klimant, *J. Photochem. Photobiol., A*, 2009, **201**, 128.
19 Y. Liu, H. Guo and J. Zhao, *Chem. Commun.*, 2011, **47**, 11471.
20 Y. Xing, C. Liu, J.-H. Xiu and J.-Y. Li, *Inorg. Chem.*, 2015, **54**, 7783.
21 P. Lehner, C. Staudinger, S. M. Borisov and I. Klimant, *Nat. Commun.*, 2014, **5**, 4460.
22 O. S. Wolfbeis, *J. Mater. Chem.*, 2005, **15**, 2657.
23 M. Quaranta, S. M. Borisov and I. Klimant, *Bioanal. Rev.*, 2012, **4**, 115.
24 V. V. Vasil'ev and S. M. Borisov, *Sens. Actuators, B*, 2002, **82**, 272.
25 T. Ishiji, K. Kudo and M. Kaneko, *Sens. Actuators, B*, 1994, **22**, 205.
26 Y. Amao, K. Asai, T. Miyashita and I. Okura, *Polym. Adv. Technol.*, 2000, **11**, 705.
27 Y. Amao, K. Asai, I. Okura, H. Shinohara and H. Nishide, *Analyst*, 2000, **125**, 1911.
28 Y. Amao, T. Miyashita and I. Okura, *Anal. Chim. Acta*, 2000, **421**, 167.
29 W. Wu, W. Wu, S. Ji, H. Guo and J. Zhao, *Dalton Trans.*, 2011, **40**, 5953.
30 W. Wu, J. Sun, S. Ji, W. Wu, J. Zhao and H. Guo, *Dalton Trans.*, 2011, **40**, 11550.
31 C. Liu, X. Song, Z. Wang and J. Qiu, *ChemPlusChem*, 2014, **79**, 1472.
32 C. Liu, X. Song, X. Rao, Y. Xing, Z. Wang, J. Zhao and J. Qiu, *Dyes Pigm.*, 2014, **101**, 85.
33 Y. Xing, C. Liu, X. Song and J. Li, *J. Mater. Chem. C*, 2015, **3**, 2166.
34 L. Deng, T. Zhang, R. Wang and J. Li, *J. Mater. Chem.*, 2012, **22**, 15910.
35 J. Li, R. Wang, R. Yang, W. Zhou and X. Wang, *J. Mater. Chem. C*, 2013, **1**, 4171.
36 J. Li, T. Zhang, Y. Liang and R. Yang, *Adv. Funct. Mater.*, 2013, **23**, 619.
37 N. Li, Y. Fang, L. Li, H. Zhao, Y. Quan, S. Ye, Q. Fan and W. Huang, *J. Lumin.*, 2018, **199**, 465.
38 J. Hu, X. Zhang, D. Zhang, X. Cao, T. Jiang, X. Zhang and Y. Tao, *Dyes Pigm.*, 2017, **137**, 480.
39 P. Agarwala and D. Kabra, *J. Mater. Chem. A*, 2017, **5**, 1348.
40 R. Maragani, R. Misra, M. S. Roy, M. K. Singh and G. D. Sharma, *Phys. Chem. Chem. Phys.*, 2017, **19**, 8925.
41 S. Soman, S. C. Pradhan, M. Yoosuf, M. V. Vinayak, S. Lingamoorthy and K. R. Gopidas, *J. Phys. Chem. C*, 2018, **122**, 14113.

42 L. Di, Y. Xing, X. Wang, D. Zheng, Y. Yang and F. Li, *RSC Adv.*, 2018, **8**, 41040.
43 J. Zhao, W. Wu, J. Sun and S. Guo, *Chem. Soc. Rev.*, 2013, **42**, 5323.
44 Q. Li, C. Shi, M. Huang, X. Wei, H. Yan, C. Yang and A. Yuan, *Chem. Sci.*, 2019, **10**, 3257.
45 W. Wu, H. Guo, W. Wu, S. Ji and J. Zhao, *Inorg. Chem.*, 2011, **50**, 11446.
46 W. Wai-SanáLee and K. ShingáChan, *J. Mater. Chem.*, 1993, **3**, 1031.
47 W. Wu, J. Sun, X. Cui and J. Zhao, *J. Mater. Chem. C*, 2013, **1**, 4577.
48 E. Carraway, J. Demas and B. DeGraff, *Langmuir*, 1991, **7**, 2991.
49 T. Lu and F. Chen, *J. Comput. Chem.*, 2012, **33**, 580.
50 W. Humphrey, A. Dalke and K. Schulten, *J. Mol. Graphics*, 1996, **14**, 33.
51 S. M. Borisov, R. Pommer, J. Svec, S. Peters, V. Novakova and I. Klimant, *J. Mater. Chem. C*, 2018, **6**, 8999.